X 62 64676

[redacted]

Copy 440
RM L58A17a

NACA RM L58A17a

Declassified by authority of NASA
Classification Change Notices No. 181
Dated ** 8/15/69

X80K-04

NACA

RESEARCH MEMORANDUM

SOME EXPERIMENTAL HEATING DATA ON CONVEX AND CONCAVE HEMISPHERICAL NOSE SHAPES AND HEMISPHERICAL DEPRESSIONS ON A 30° BLUNTED NOSE CONE

By Russell N. Hopko and H. Kurt Strass

Langley Aeronautical Laboratory
Langley Field, Va.

[redacted]

X69-76940
(ACCESSION NUMBER) (THRU)
33 NONE
(PAGES) (CODE)
(NASA CR OR TMX OR AD NUMBER) (CATEGORY)
FF No. 602(D)
AVAILABLE TO NASA OFFICES AND CONTRACTORS ONLY
Restriction/Classification Cancelled

[redacted]

of the espionage laws, Title 18, U.S.C., Secs. 793 and 794. Its transmission or the revelation of its contents in any manner to an unauthorized person is prohibited by law.

NATIONAL ADVISORY COMMITTEE FOR AERONAUTICS

WASHINGTON
March 10, 1958

[redacted]

[redacted]

NATIONAL ADVISORY COMMITTEE FOR AERONAUTICS

Declassified by authority of NASA
Classification Change Notices No. 181
Dated ** 3/25/67

RESEARCH MEMORANDUM

SOME EXPERIMENTAL HEATING DATA ON CONVEX AND CONCAVE HEMISPHERICAL NOSE SHAPES AND HEMISPHERICAL DEPRESSIONS ON A 30° BLUNTED NOSE CONE

By Russell N. Hopko and H. Kurt Strass

SUMMARY

Some experimental heating data on concave and convex hemispherical nose shapes and hemispherical depressions on a blunted 30° cone have been obtained. Data obtained at Mach numbers up to approximately 8.5 indicate that the heating of the stagnation point of a concave hemispherical nose shape is approximately one-third that of a convex hemispherical nose shape at a Mach number of 2 and approximately one-tenth that of a convex hemispherical nose shape at a Mach number of 8.

INTRODUCTION

The advent of the intercontinental ballistic missile (ICBM) has caused emphasis to be placed on nose shapes conducive to high drag and low aerodynamic heat transfer (refs. 1 to 3). Results of several recently completed tests reported herein have contributed data concerning the relative heating within concave and on convex nose shapes which may aid in minimizing the heat transfer to the nose of a ballistic missile.

The data presented herein are comparative measurements of stagnation-point skin temperatures on a convex hemispherical nose and on a concave hemispherical nose at a Mach number of 2 obtained in a laboratory-scale ceramic-heated air jet and from two rocket-model tests up to a maximum velocity of 8,500 feet per second. Stagnation-point skin temperatures on the flight models were measured simultaneously on both models which were pylon-mounted around the test vehicle. Also included herein are skin-temperature histories and heat-transfer coefficients obtained during a third flight to a Mach number of 3.2 of a

[redacted]

blunted nose cone, the surface of which had several hemispherical depressions representing damage to an ICBM nose resulting from the impact of meteorites or enemy countermeasures.

The data presented herein were obtained from four exploratory tests conducted in a laboratory-scale ceramic-heated air jet and three flight tests. Comparative measurements of skin temperature were obtained on a concave and convex hemispherical nose in two separate runs in the jet and also on similar models carried by each of two flight vehicles. Data were obtained at a Mach number of 2 in the ceramic-heated air jet and at Mach numbers up to 8.5 in flight.

SYMBOLS

c	specific heat of skin
h	heat-transfer coefficient
M	Mach number
N_{Pr}	Prandtl number
T	temperature
t	time
w	density of wall
τ	skin thickness

Subscripts:

aw	adiabatic wall
w	wall
S	stagnation

MODELS AND TECHNIQUES

The models and test vehicles used in this investigation are described in figures 1 to 11 by means of photographs and dimensional sketches. Models 1 and 2 were tested in the laboratory-scale

ceramic-heated air jet. Models 3 to 7 were tested in flight using multistage rocket-powered vehicles. All of the models were instrumented with thermocouples welded to the inner surface.

Hot-Jet Tests

Cross-sectional views of the two nose shapes (models 1 and 2) tested in the ceramic-heated air jet are shown in figure 1. The models were made of Inconel and had platinum—platinum-rhodium thermocouples welded to the inner surface at the stagnation point. Model 1 was a $\frac{3}{8}$-inch-diameter convex hemispherical nose and model 2 was a concave hemispherical nose $\frac{5}{16}$ inch in diameter. The manner in which the models are mounted for testing in the hot jet is illustrated in the photograph presented as figure 2. Figure 3 shows details of the model assembly and supporting pylon. The same arrangement was used to support the models tested on the flight vehicles.

The air jet operates at a Mach number of approximately 2, and for these tests the stagnation temperature was approximately 3,500° F. The models were inserted into the jet and removed from the jet by means of a quick-acting pneumatic mechanism. More detailed information regarding the laboratory-scale ceramic-heated air jet may be obtained from reference 4.

Flight Tests

The principal instrumentation of the flight models consisted of thermocouples. The outputs from the thermocouples, in conjunction with three reference voltages, were commutated in order that several thermocouple outputs might be transmitted over one telemeter channel. The reference voltages were obtained by the use of a mercury cell and a voltage-dividing network designed to supply a range of voltages equivalent to the temperature range that the thermocouples were expected to cover. The reference voltages provided a method for checking the calibration of the telemetry system in flight.

True air velocity data were obtained by correcting the velocity measured by a CW Doppler velocimeter for angular deviation of the flight path relative to the radar transmitter and for winds at altitude by the use of model space coordinates measured by an NACA modified SCR-584 tracking radar. Atmospheric and wind conditions were obtained by radiosondes launched immediately after the test flight and tracked by a Rawin set AN/GMD-1A. The test vehicle carrying models 5 and 6 exceeded

the Doppler radar range, and velocity was obtained by integrating the telemetered acceleration.

Models 3, 4, 5, and 6, which are shown in figure 1, were tested (in conjunction with other models not related to this investigation) on two identical four-stage rocket vehicles. A photograph showing the propulsion system employed is presented as figure 4. The models were pylon-mounted around the cylindrical portion of the vehicles, 30 inches from the nose as illustrated in the photographs presented as figures 5 and 6. Details of the mounting pylons are shown in figure 3. Models 3 and 4 were mounted on one of the test vehicles and models 5 and 6 were mounted on the other. Models 3 and 4 were made of mild steel but were otherwise identical to hot-jet models 1 and 2, respectively, which were made of Inconel. Models 5 and 6 were also made of Inconel. Model 5 was constructed with a variation skin thickness designed to minimize heat conduction near the stagnation point according to theoretical laminar-flow considerations. On each model, the skin temperature at the stagnation point was measured by thermocouples welded to the inner surface of the skin.

From the flight test of models 3 and 4, data were obtained only during the initial portion of the flight since telemeter failure at the end of burning of the second stage precluded further measurements. The data for models 3 and 4 are limited to a maximum Mach number of approximately 4. Altitude and velocity histories for the vehicle carrying these models are presented in figure 12. Data obtained on models 5 and 6 at test-vehicle speeds up to 8,400 feet per second are presented in figure 13.

Model 7 was a blunted nose cone having a half-angle of 15° and was equipped with five $\frac{3}{8}$- inch-diameter hemispherical depressions arranged along the surface as shown in figures 7 and 8. The depressions were intended to simulate the surface damage to a reentry nose resulting from meteoritic impact or enemy countermeasures. The model was constructed of 0.027-inch-thick Inconel and employed a stabilized high-emissivity surface coating applied according to the procedure given in reference 5. The surface finish was approximately 30 microinches root mean square, as measured by a Brush surface analyzer. Not shown in figure 7 is an inner reinforcing cone of an insulator in contact with the Inconel skin. The insulator was cut away sufficiently to allow at least $\frac{3}{16}$- inch clearance in the vicinity of the thermocouples and the hemispherical depressions in order to minimize heat losses to the insulator in the region of the measuring point. Errors in heat-transfer coefficient due to conduction effects were estimated to be less than 10 percent and were neglected. The nose cone was equipped with

18 thermocouples installed as shown in figure 9. The commutation rate was such that thermocouples 1 to 5 and 13 could be read approximately 10 times a second. Thermocouples 6 to 12, 14 to 18, and the three reference voltages could be read approximately 5 times a second.

The test vehicle for model 7 is described in the photographs presented as figures 10 and 11. A three-stage propulsion system was used which was designed to propel the model to approximately $M = 7$, but a structural failure of the booster assembly occurred immediately after burnout of the first stage and thus prematurely disengaged the instrumented third stage. The structural failure of the booster also prevented the third-stage rocket motor from firing and limited the maximum Mach number to approximately 3.2. Careful study of both the telemeter records and motion pictures made with tracking cameras failed to reveal any evidence of damage to the instrumented last stage. The measured flight performance data for this vehicle are presented in figure 14.

RESULTS AND DISCUSSION

Convex and Concave Nose Tests

Hot-jet tests.- The temperature histories obtained at the stagnation points of models 1 and 2 in the laboratory-scale ceramic-heated air jet are shown in figure 15. The initial slopes of the curves reflect the relative aerodynamic heat input. It appears that the heat transfer to the stagnation point of the concave nose is approximately one-third that transferred to the convex-nose stagnation point. At high model temperatures, heat-conduction effects are large; however, figure 15 shows that significantly less heat has been transferred to the stagnation point of the concave nose.

Flight tests.- The temperature histories obtained in flight with models 3 and 4 are shown in figure 16. The temperature histories obtained with models 5 and 6 are shown in figure 17. The center lines of these models were approximately $\frac{3}{4}$ inch above the surface of the test vehicle. Although the models were not in free-stream flow, comparative models were subjected to similar environments. Again, as in the jet tests, the lower heat-transfer characteristics at the stagnation point of the concave nose shape are quite evident in both the heating and cooling portions of the flight histories of the models.

The slopes of the history curves reflect the heat transfer to the nose shapes. From figures 15, 16, and 17 it appears that at $M = 2$

the heat transfer to the stagnation point (model center line) of the concave hemisphere is approximately one-third that of the convex hemisphere and at $M = 8$ ($t = 105$ seconds), the heat transfer to the stagnation point of the concave hemisphere is approximately one-tenth that of the convex hemisphere.

Nose With Hemispherical Depressions

The variation of the measured skin temperatures with time for model 7 is presented in figure 18. The curves are arranged in groups to allow ready comparison of the temperatures within the hemispherical depressions with temperatures at comparable locations on the smooth surface. It should be noted that, in figure 18(a), the temperature rise within the hemispherical depression located at the stagnation point (thermocouples 1 and 2) was much less than that measured on the smooth surface immediately adjacent to the depression (thermocouple 13). With the exception of thermocouple 7 (fig. 18(c)), the remainder of the thermocouples within the depressions exhibited temperature rises equal to or greater than thermocouples located at comparable locations on the smooth surface.

The temperature measurements were reduced to heat-transfer coefficients by using the thin-wall formula

$$h = \frac{c w \tau}{T_{aw} - T_w} \frac{dT_w}{dt}$$

The value of $\frac{dT_w}{dt}$ was calculated by employing a curve-fitting process wherein a third-order polynomial of unknown coefficients was fitted through nine data points (four to each side of the desired point) with the use of the method of least squares. The coefficients of the polynomial were obtained by simultaneous solution. The slope was then calculated at the center point by differentiation of the resulting polynomial. This work was performed on an IBM 650 digital computer.

The adiabatic-wall temperature T_{aw} was calculated by assuming a laminar recovery factor of $N_{Pr}^{1/2}$ based on wall temperature for all locations except the stagnation point (thermocouples 1 and 2) where the recovery factor was assumed equal to 1. Radiation and conduction effects were estimated and found to be negligible for the times for which data are presented.

Figure 19 presents the experimental heat-transfer coefficients plotted in the form of pictorial graphs for two typical times during the test. The magnitude of the heat-transfer coefficient is proportional to the distance of the plotted value measured normal to the external contour line of the blunted nose cone. Also plotted in figure 19 for comparison are theoretical laminar and turbulent values for the smooth surface based on local conditions just outside the boundary layer. The theoretical laminar heat-transfer coefficient at the stagnation point was calculated by the method of reference 2. The laminar heat-transfer coefficients over the hemispherical portion of the nose other than the stagnation point was calculated from the theory of reference 6. Theoretical laminar and turbulent values over the conical portion of the nose were calculated by the method for conical surfaces in reference 7, where the local Reynolds number was based on the distance along the surface measured from the stagnation point.

The measured stagnation-point heat-transfer coefficient within the depression was only a small fraction of the laminar theoretical value. The magnitude of interference effects of upstream depressions upon the heat transfer are unknown. The spacing of these depressions as shown in figure 7 was intended to minimize any interference effects which may have existed. However, there is the possibility that turbulent flow existed in the region of the downstream depressions; thus, any direct comparison of the heating rates within the depressions with values at comparable locations on the smooth surface where the existence of laminar flow was demonstrated is open to question.

The measured heat transfer in the depressions at other locations on the nose cone was either equal to or greater than that measured at comparable locations on the smooth surface.

CONCLUDING REMARKS

The experimental data presented herein show that the aerodynamic heat transfer to the stagnation point of a concave hemispherical nose shape is approximately one-third that of a convex hemispherical nose shape at a Mach number of 2 and is approximately one-tenth that of a convex hemispherical nose shape at a Mach number of 8. Research to determine in more detail the heat transfer to a concave hemispherical nose shape is indicated.

Langley Aeronautical Laboratory,
National Advisory Committee for Aeronautics,
Langley Field, Va., January 3, 1958.

REFERENCES

1. Allen, H. Julian, and Eggers, A. J., Jr.: A Study of the Motion and Aerodynamic Heating of Missiles Entering the Earth's Atmosphere at High Supersonic Speeds. NACA TN 4047, 1957. (Supersedes NACA RM A53D28.)

2. Korobkin, I., and Gruenewald, K. H.: Investigation of Local Laminar Heat Transfer on a Hemisphere for Supersonic Mach Numbers at Low Rates of Heat Flux. Jour. Aero. Sci., vol. 24, no. 3, Mar. 1957, pp. 188-194.

3. Carter, Howard S., and Bressette, Walter E.: Heat-Transfer and Pressure Distribution on Six Blunt Noses at a Mach Number of 2. NACA RM L57C18, 1957.

4. Purser, Paul E., and Hopko, Russell N.: Exploratory Materials and Missile-Nose-Shape Tests in a 4,000° F Supersonic Air Jet. NACA RM L56J09, 1956.

5. O'Sullivan, William J., Jr., and Wade, William R.: Theory and Apparatus for Measurement of Emissivity for Radiative Cooling of Hypersonic Aircraft With Data for Inconel and Inconel X. NACA TN 4121, 1957.

6. Stine, Howard A., and Wanlass, Kent: Theoretical and Experimental Investigation of Aerodynamic-Heating and Isothermal Heat-Transfer Parameters on a Hemispherical Nose With Laminar Boundary Layer at Supersonic Mach Numbers. NACA TN 3344, 1954.

7. Van Driest, E. R.: The Problem of Aerodynamic Heating. Aero. Eng. Rev., vol. 15, no. 10, Oct. 1956, pp. 26-41.

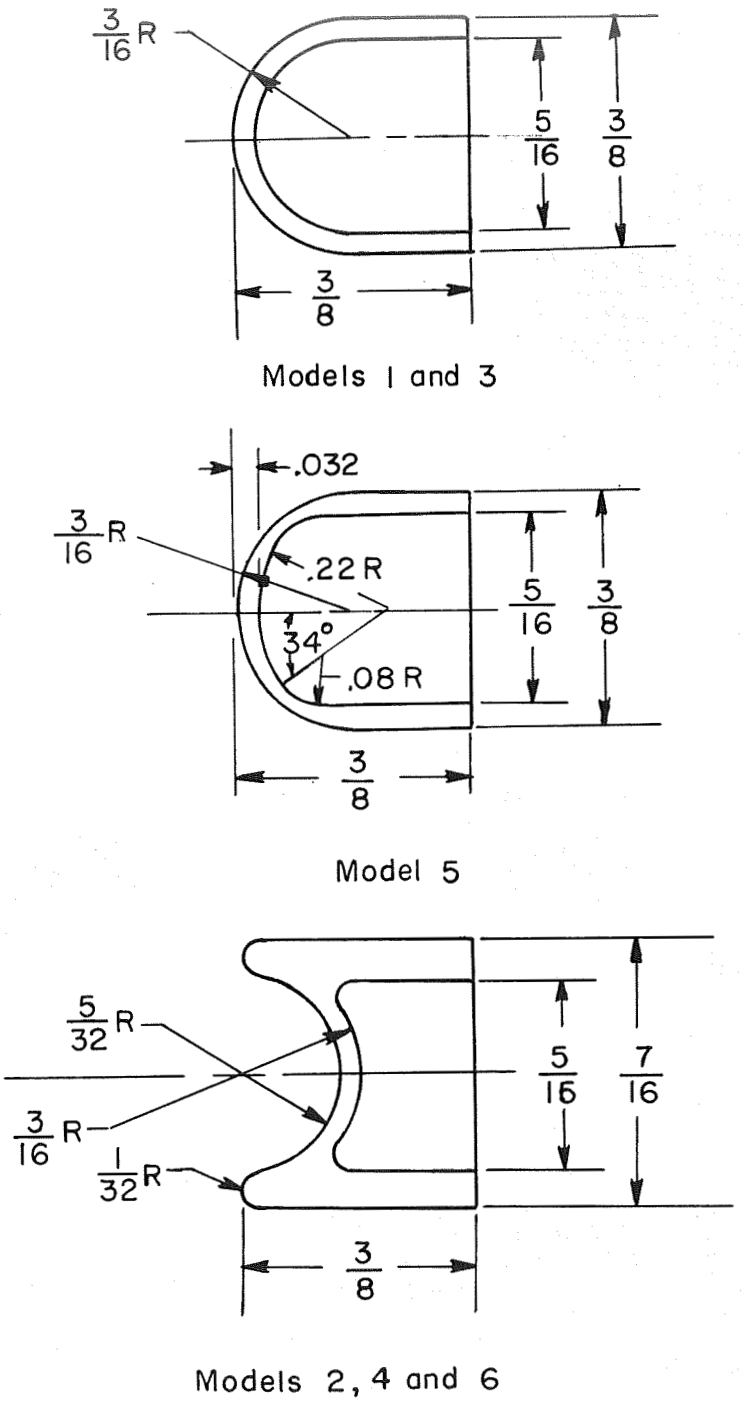

Figure 1.- Cross-sectional views of models 1 to 6. All dimensions are in inches.

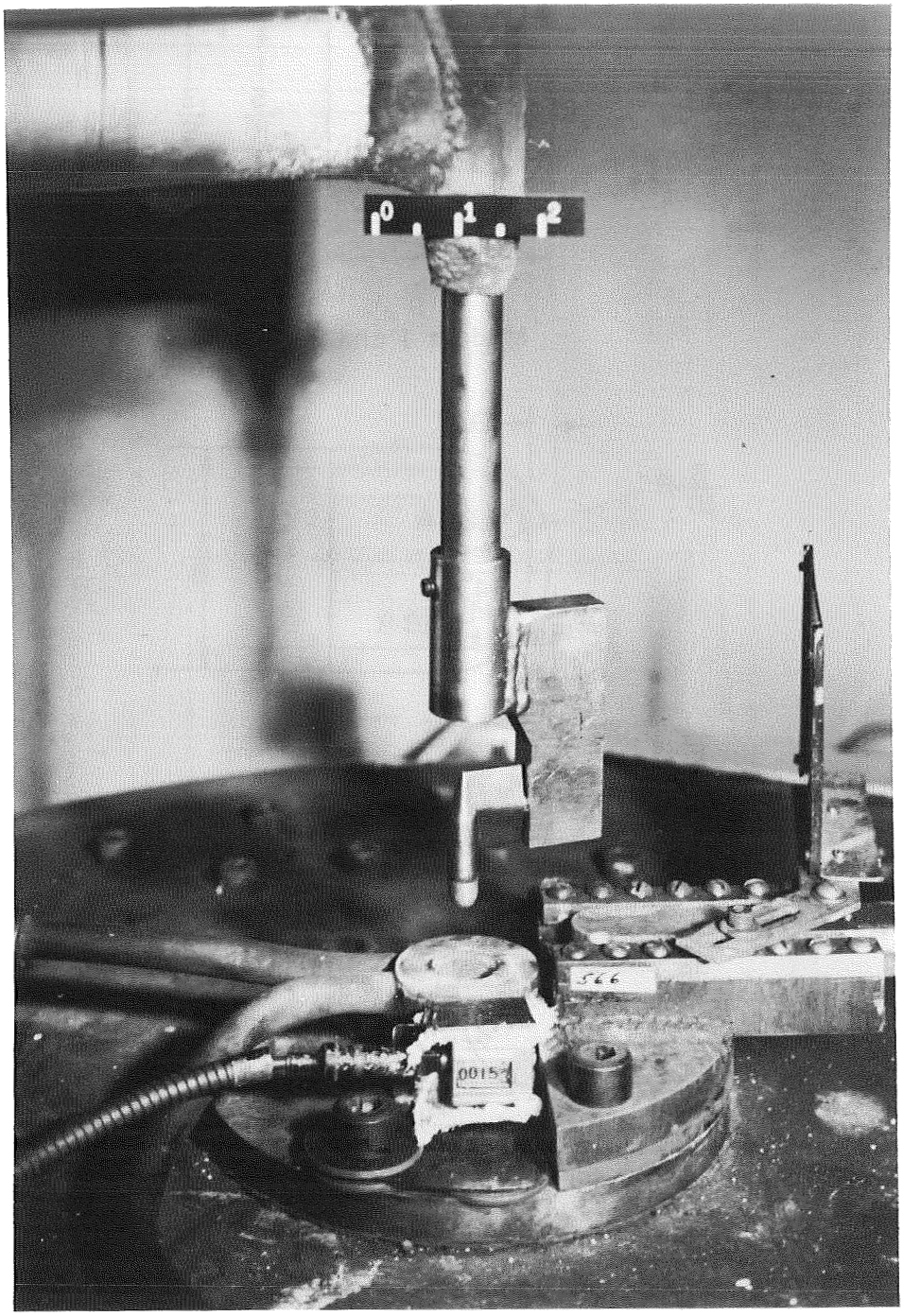

L-57-3817

Figure 2.- Photograph of model 1 in the laboratory-scale ceramic-heated air jet.

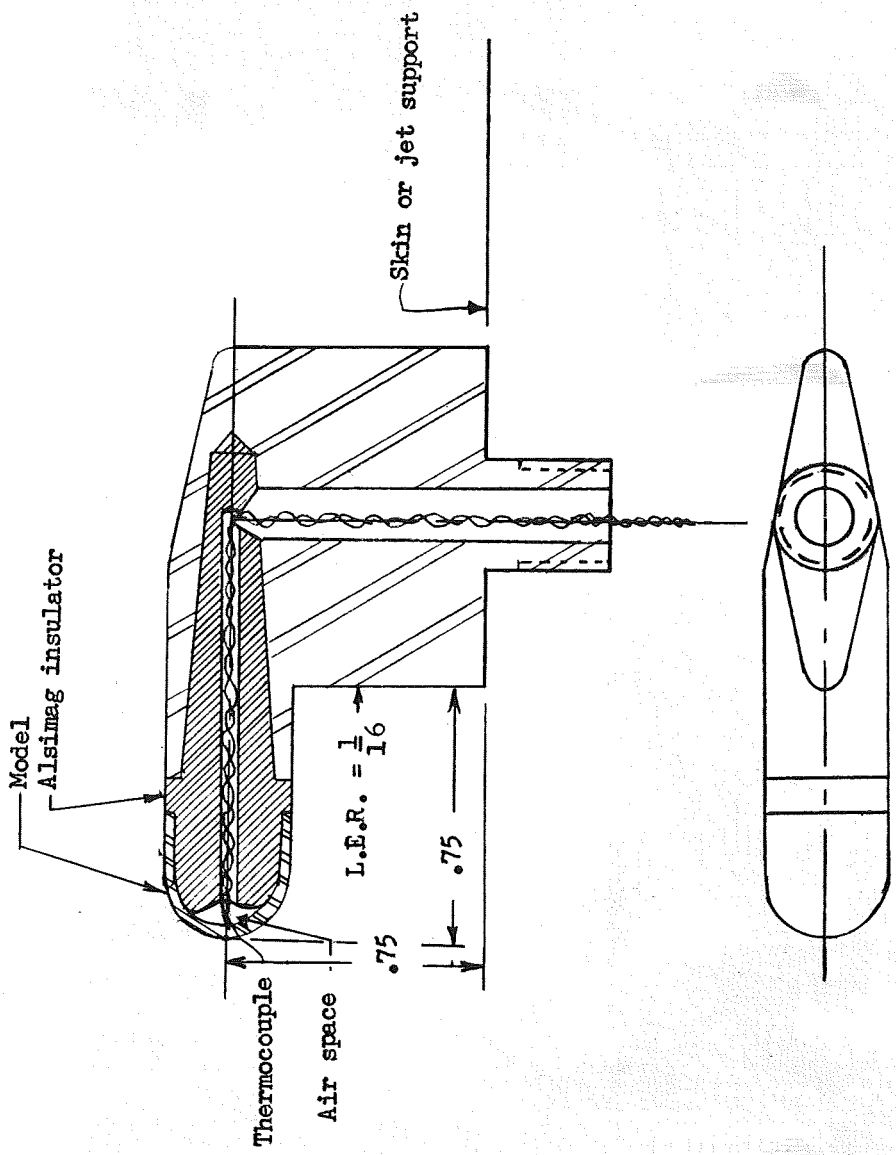

Figure 3.- Cross-sectional view of pylon-mounted models. All dimensions are in inches.

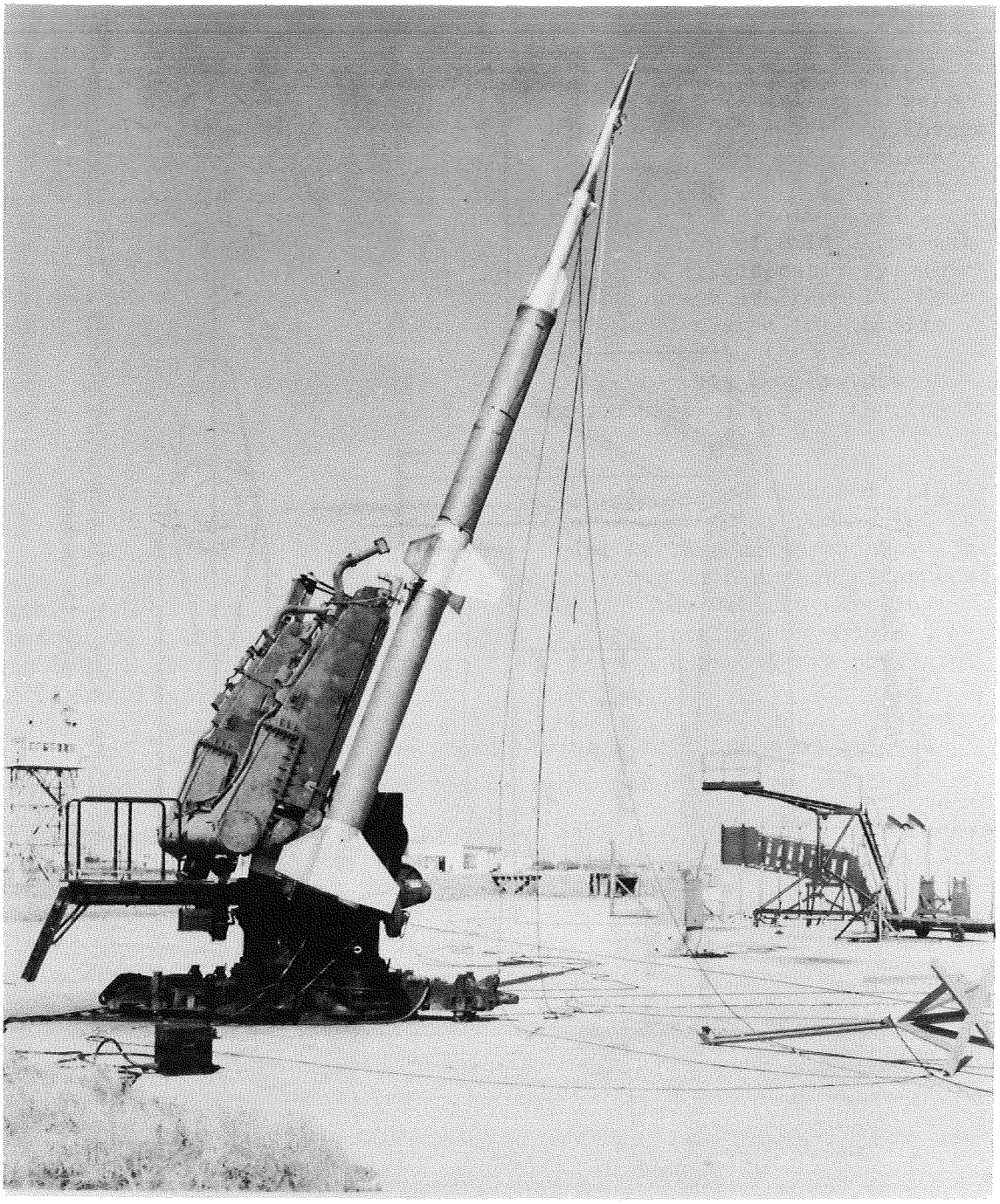

L-91338

Figure 4.- Photograph of four-stage vehicle in launching position.

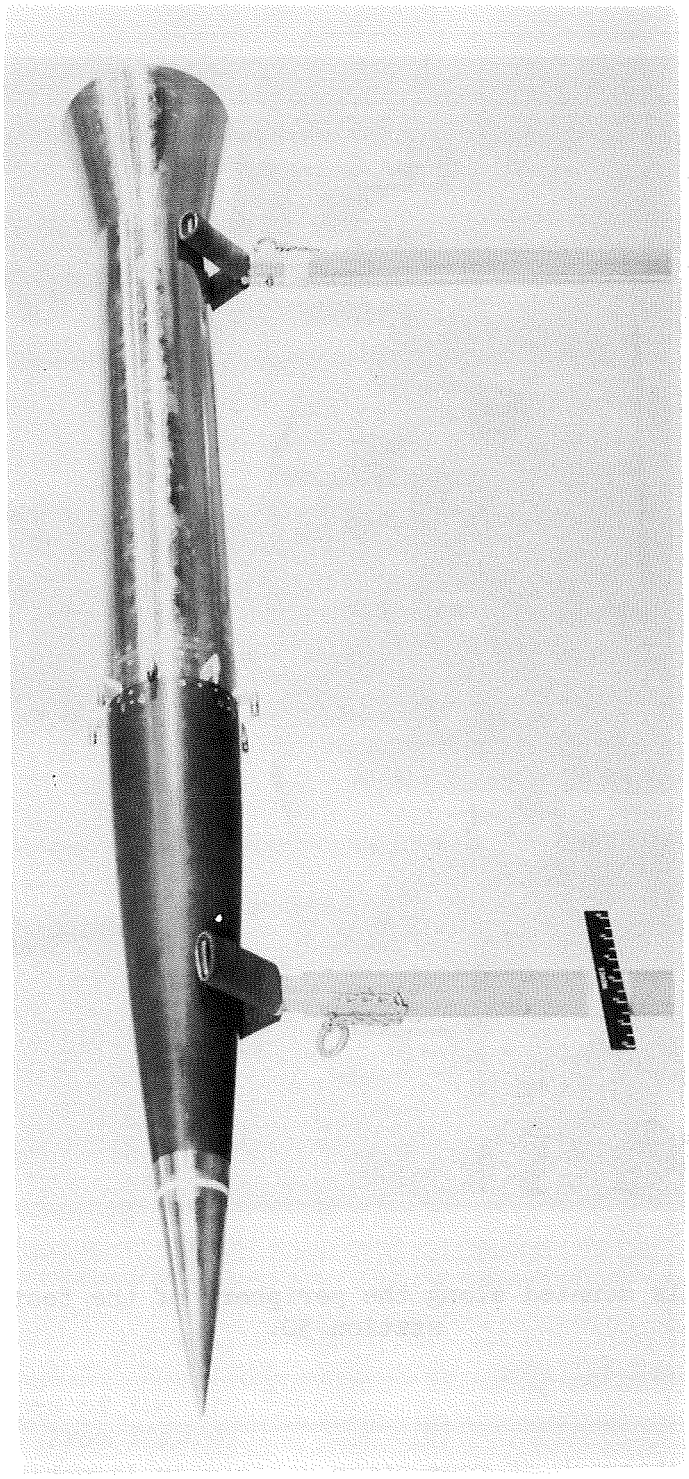

L-91101.1

Figure 5.- Three-quarter front view of test vehicle carrying models 3 and 4. Test vehicle carrying models 5 and 6 is identical.

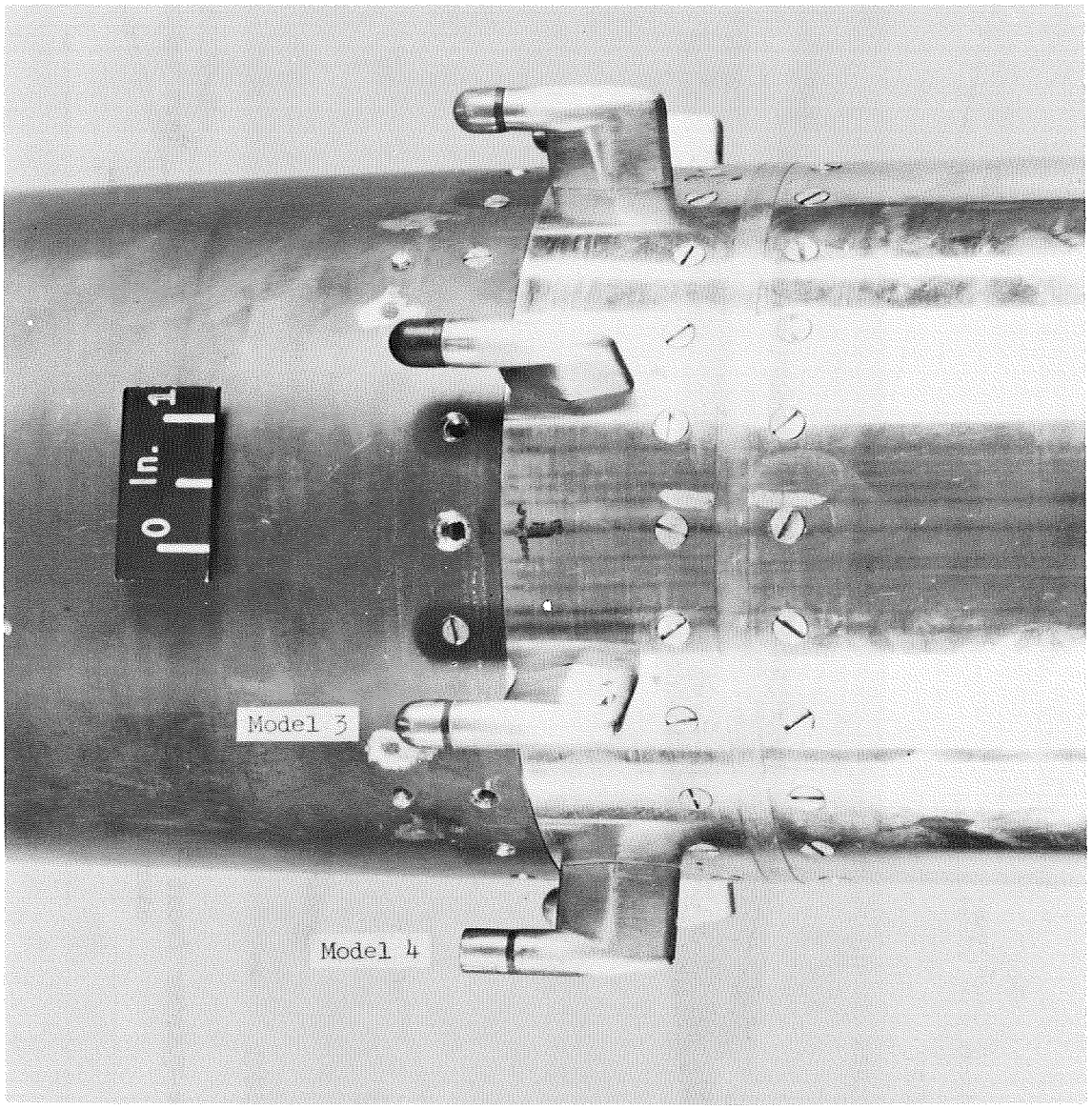

L-91102.1

Figure 6.- Models mounted along the periphery of the test vehicle at station 30.

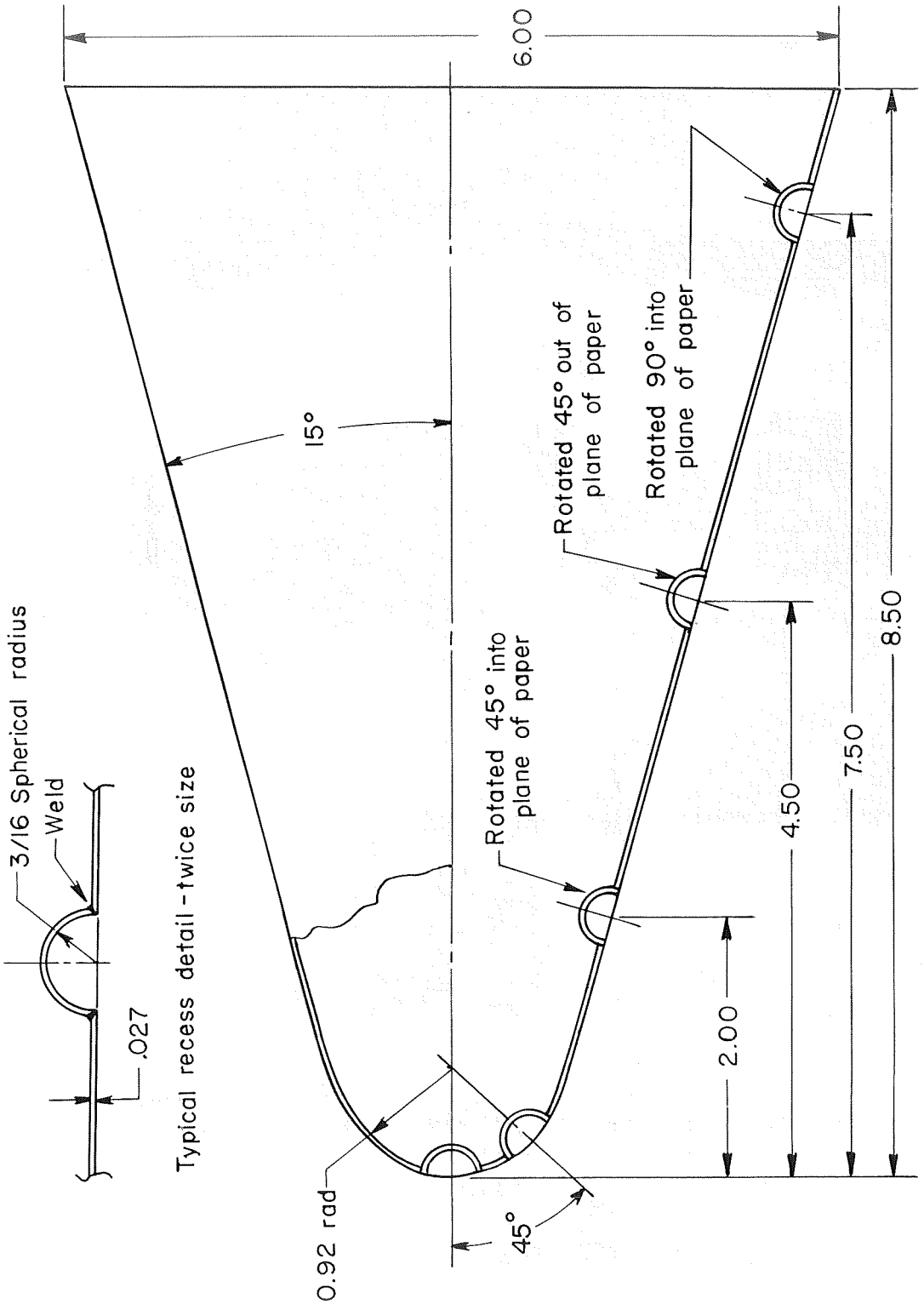

Figure 7.- General arrangement of model 7. All dimensions are in inches.

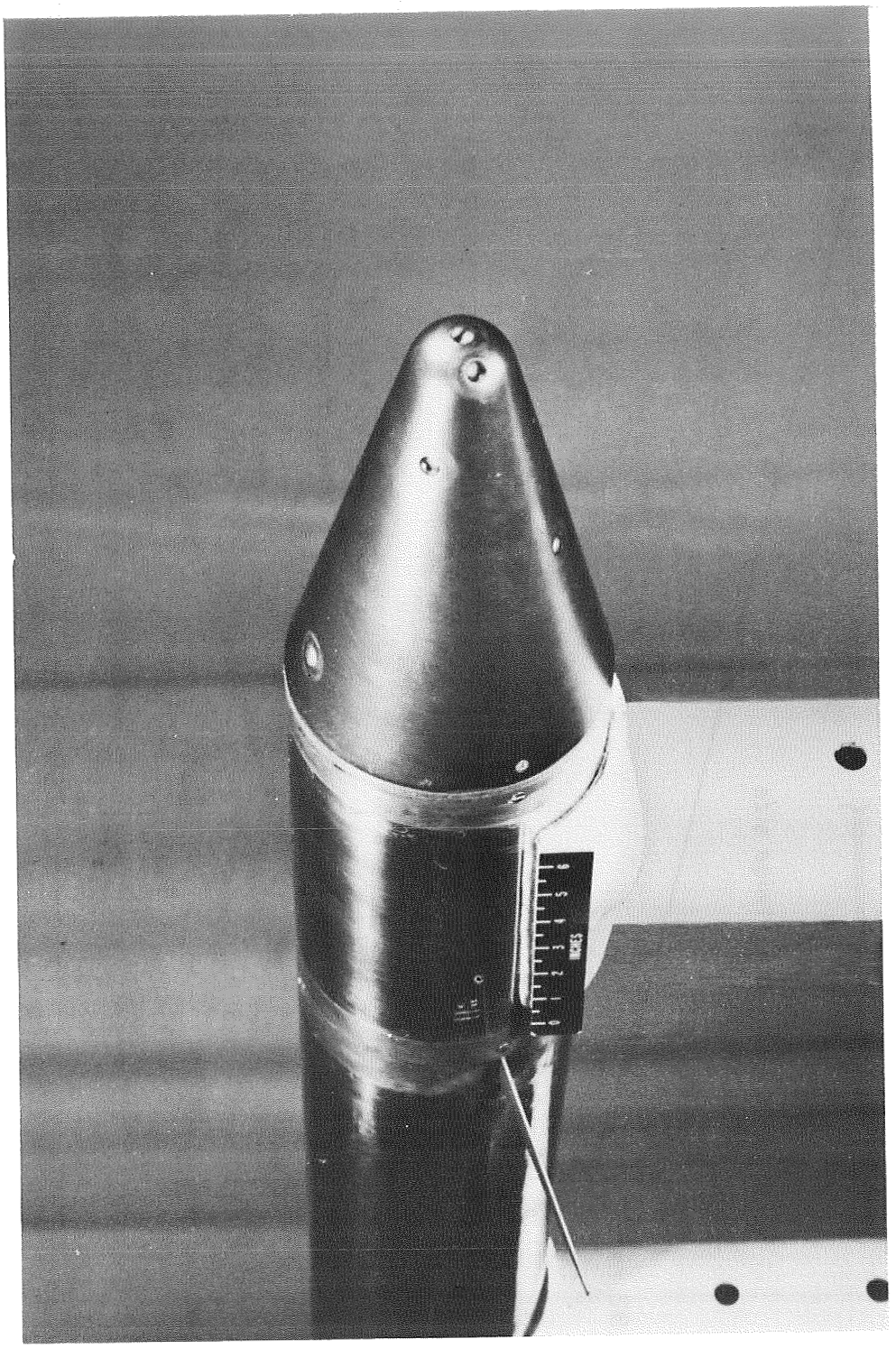

L-96969.1

Figure 8.- Three-quarter front view showing nose details of model 7.

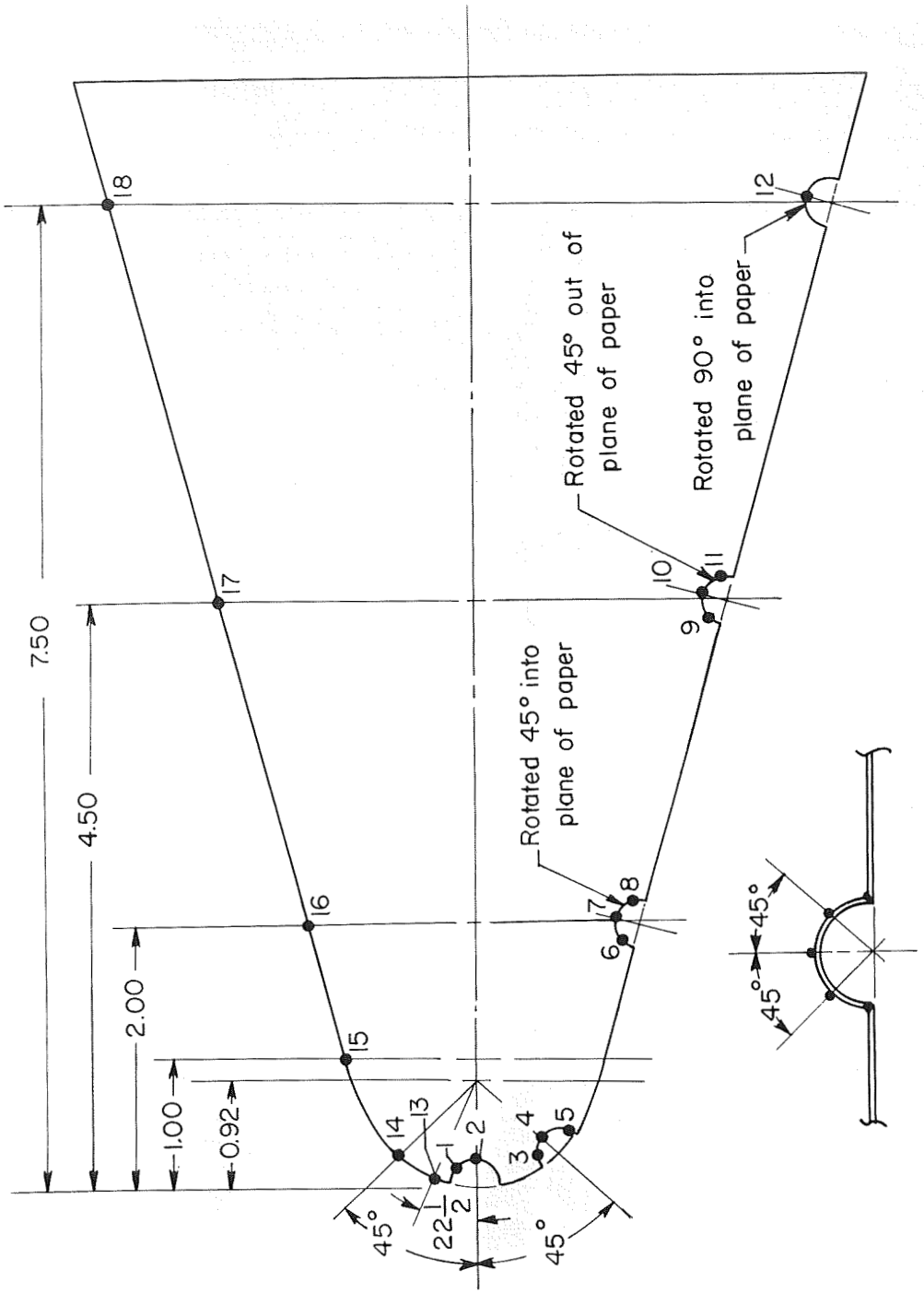

Figure 9.- Thermocouple locations on model 7. All dimensions are in inches.

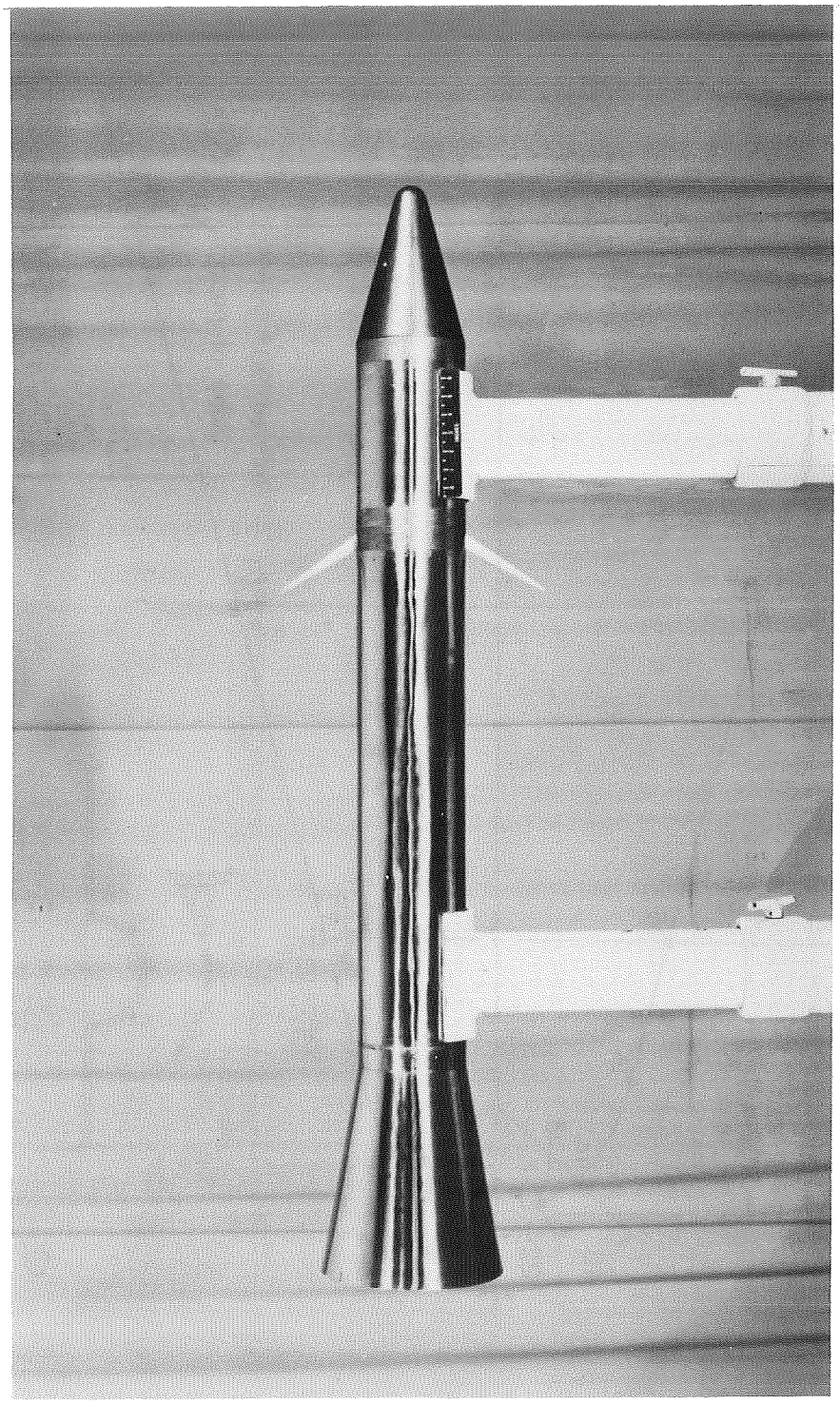

L-96972.1

Figure 10.- Side view of model 7 and the test vehicle.

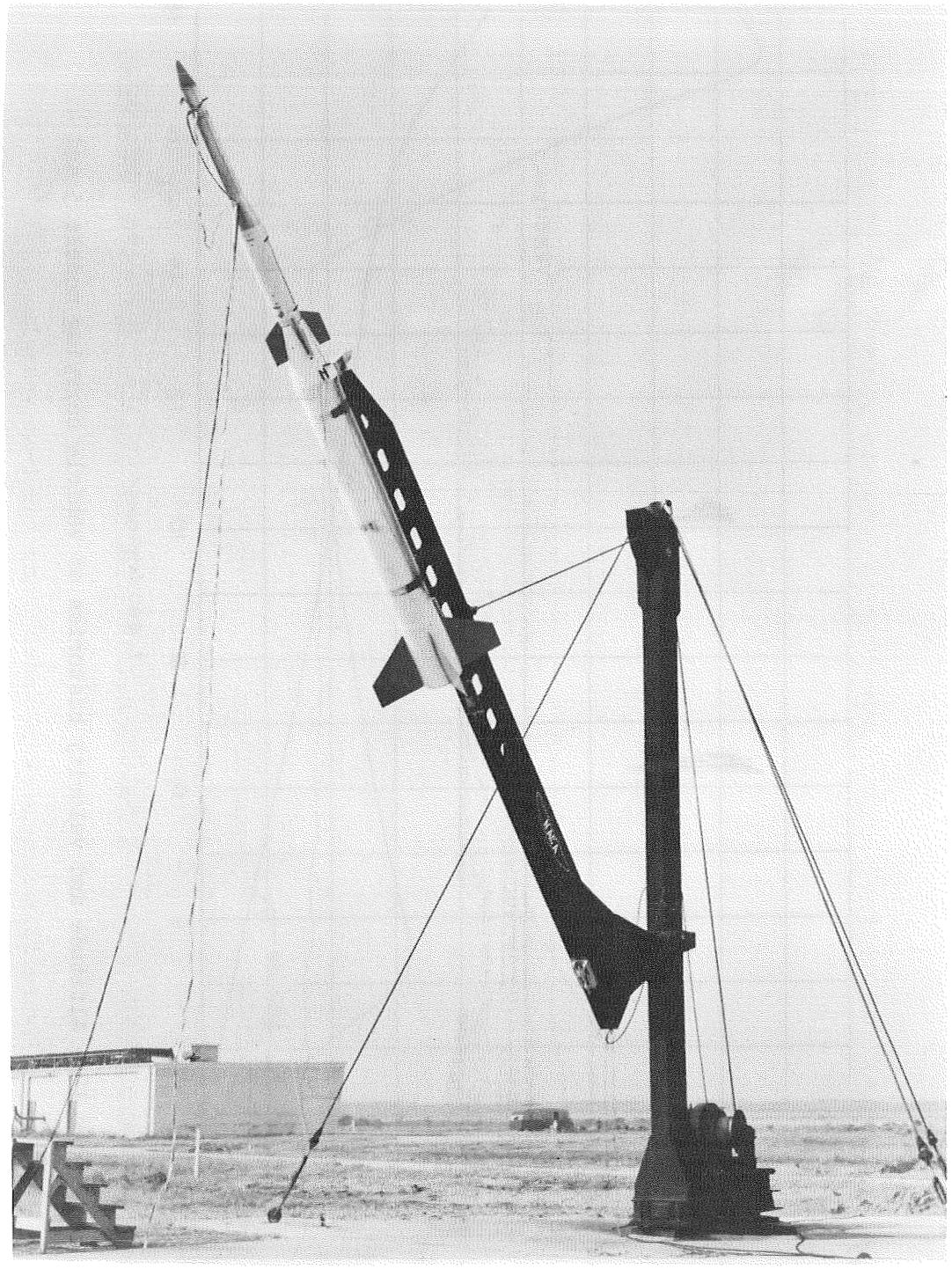

L-97085

Figure 11.- Test vehicle and boosters carrying model 7.

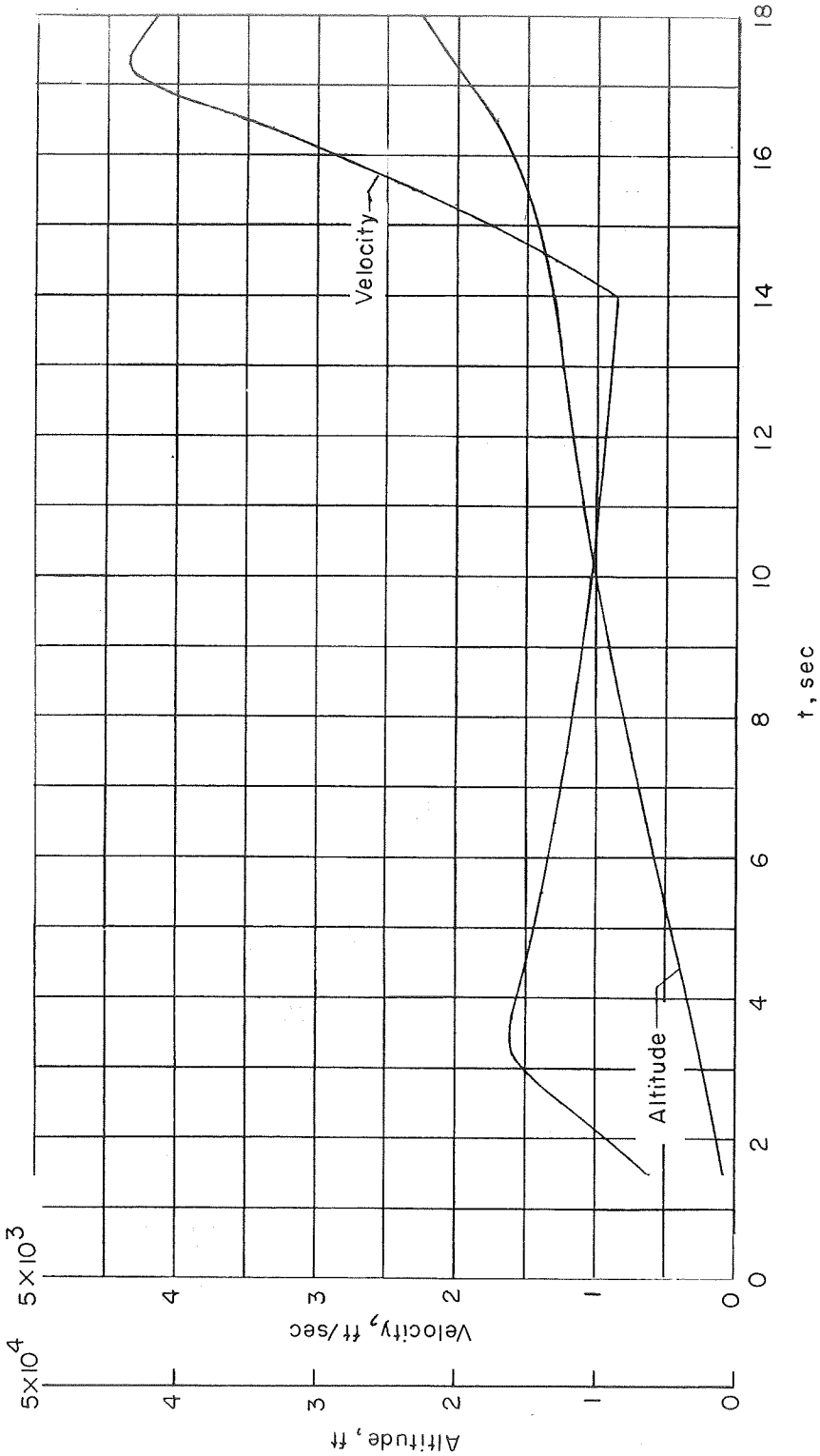

Figure 12.- Altitude and velocity histories of vehicle carrying models 3 and 4.

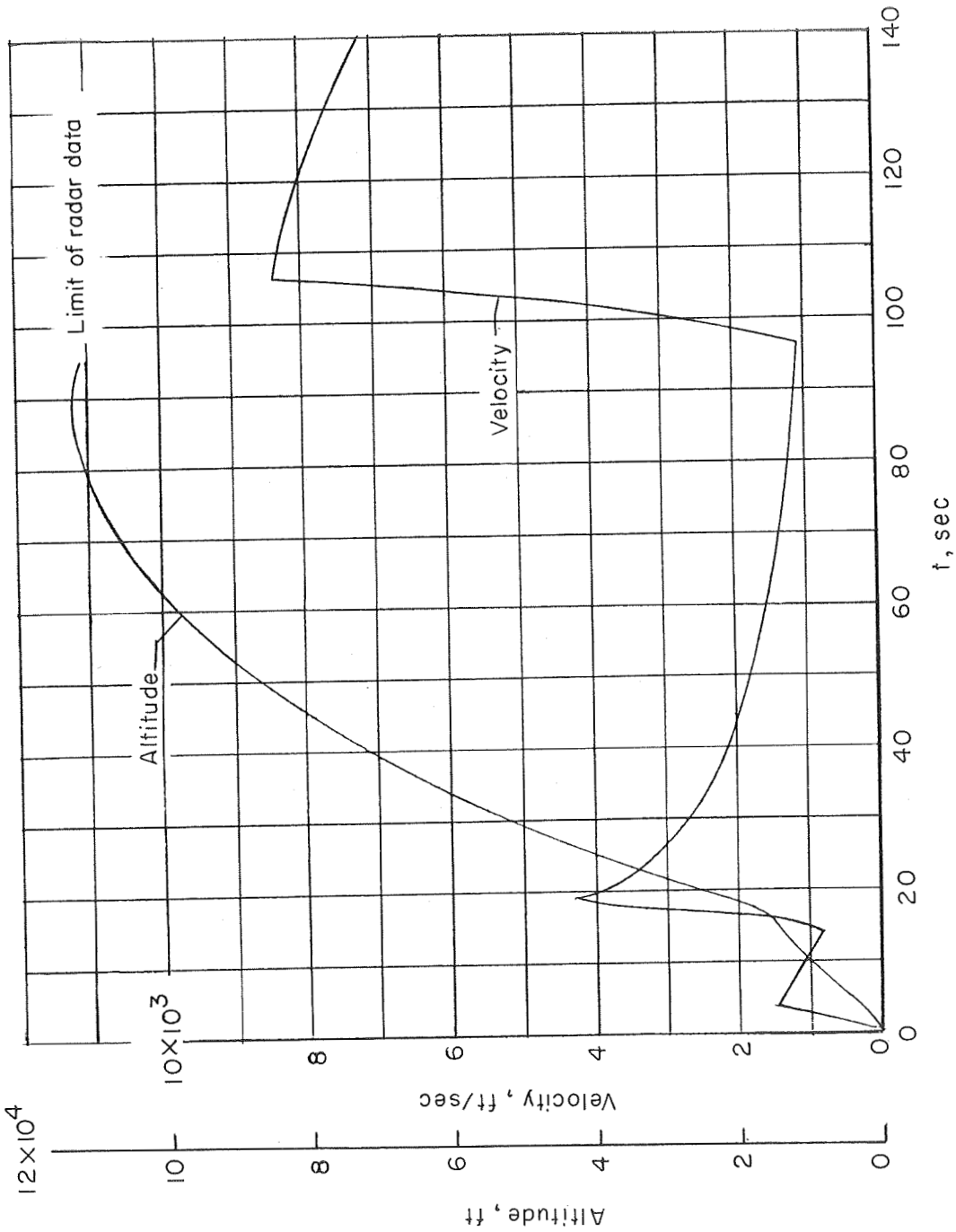

Figure 13.- Altitude and velocity histories of vehicle carrying models 5 and 6.

[redacted]

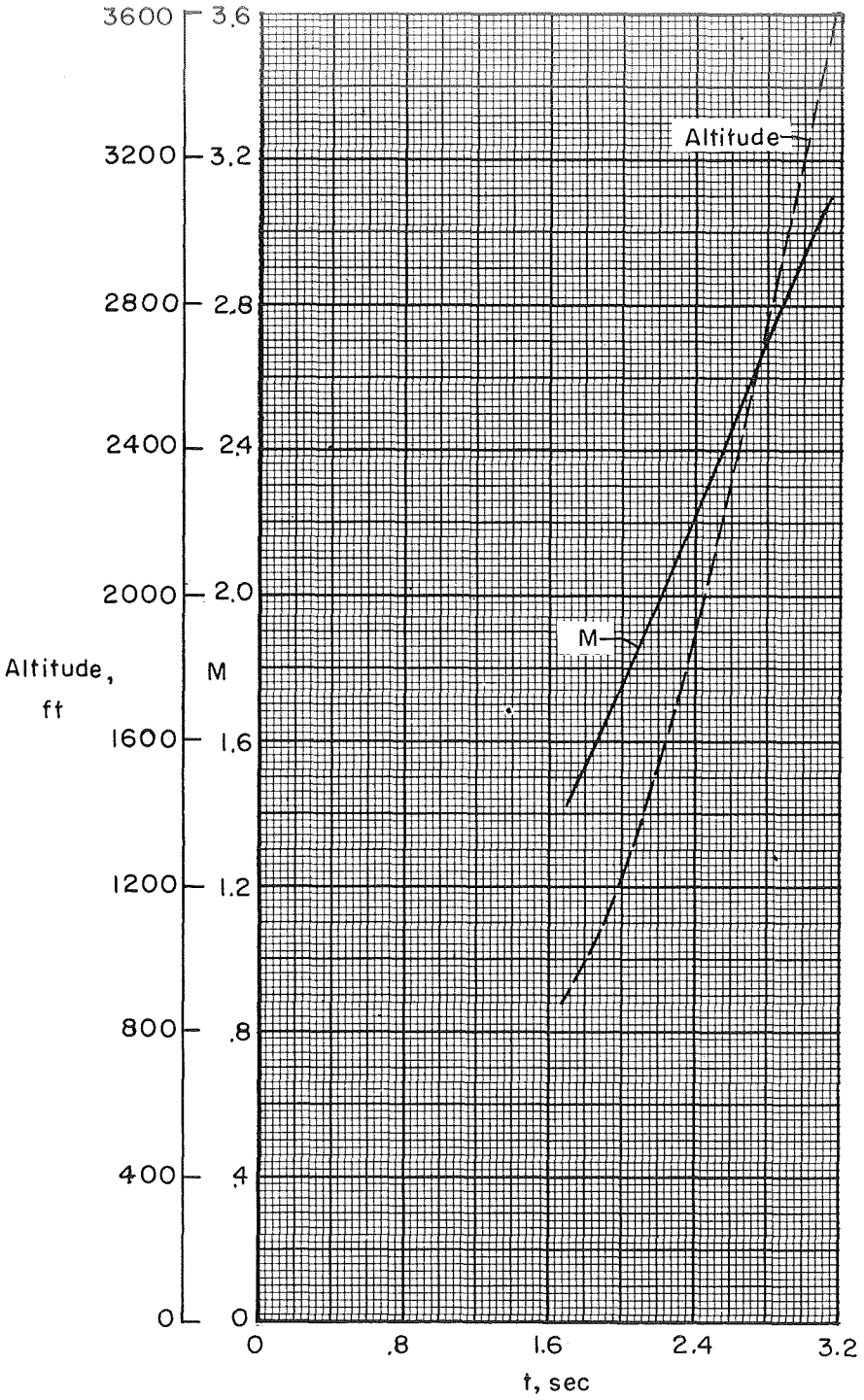

Figure 14.- Altitude and Mach number history of vehicle carrying model 7.

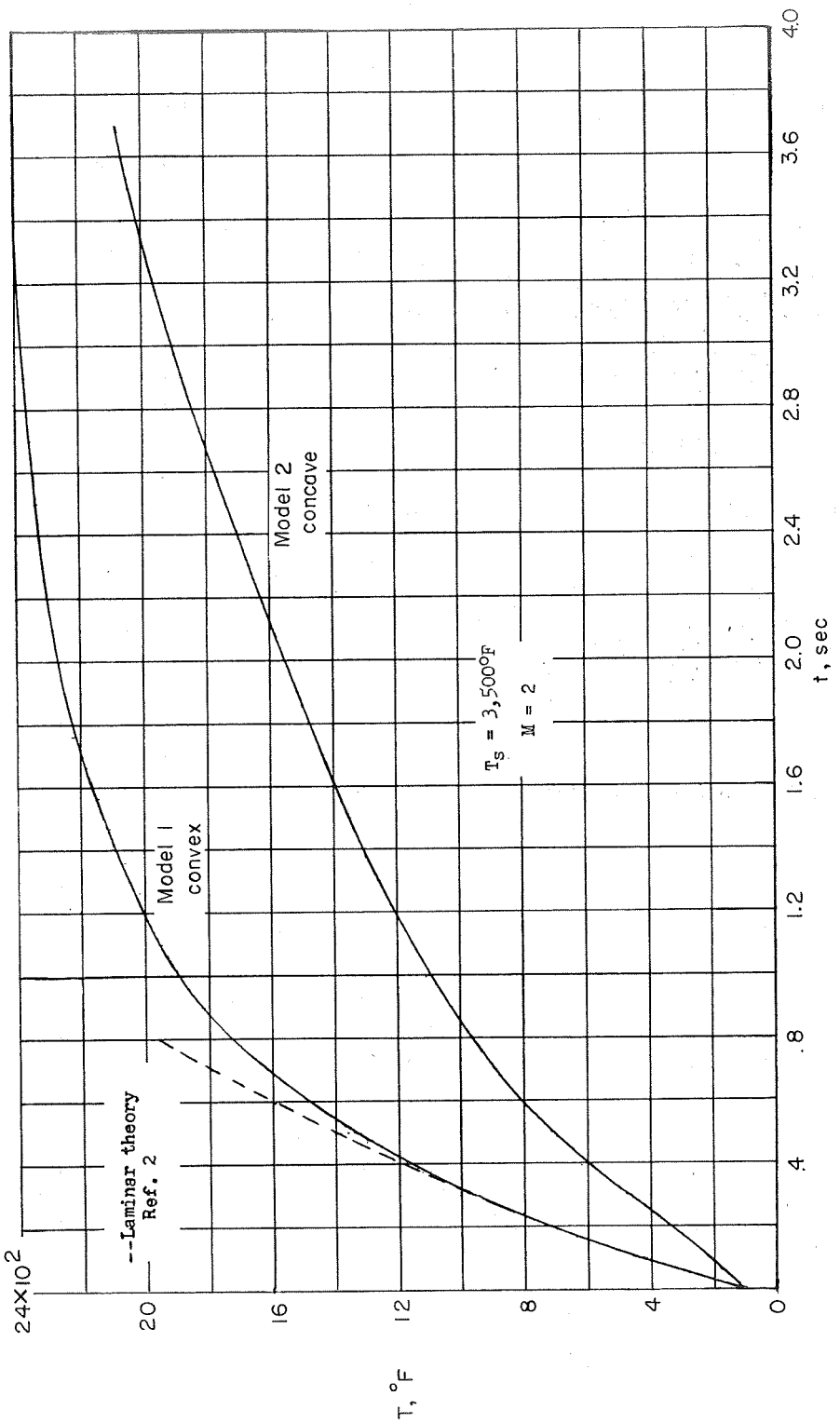

Figure 15.- Temperature histories of models 1 and 2.

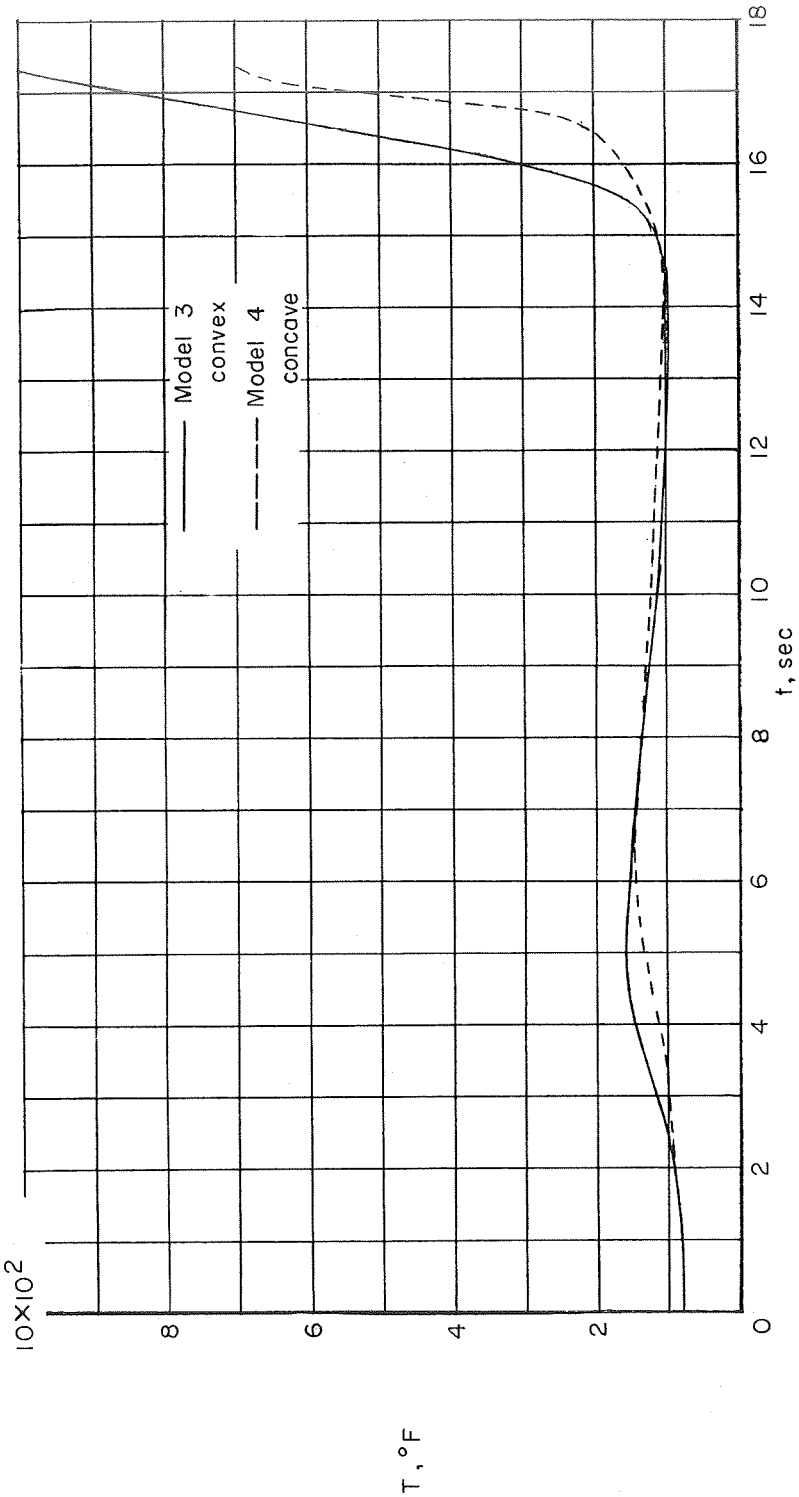

Figure 16.- Temperature histories at the stagnation points of models 3 and 4.

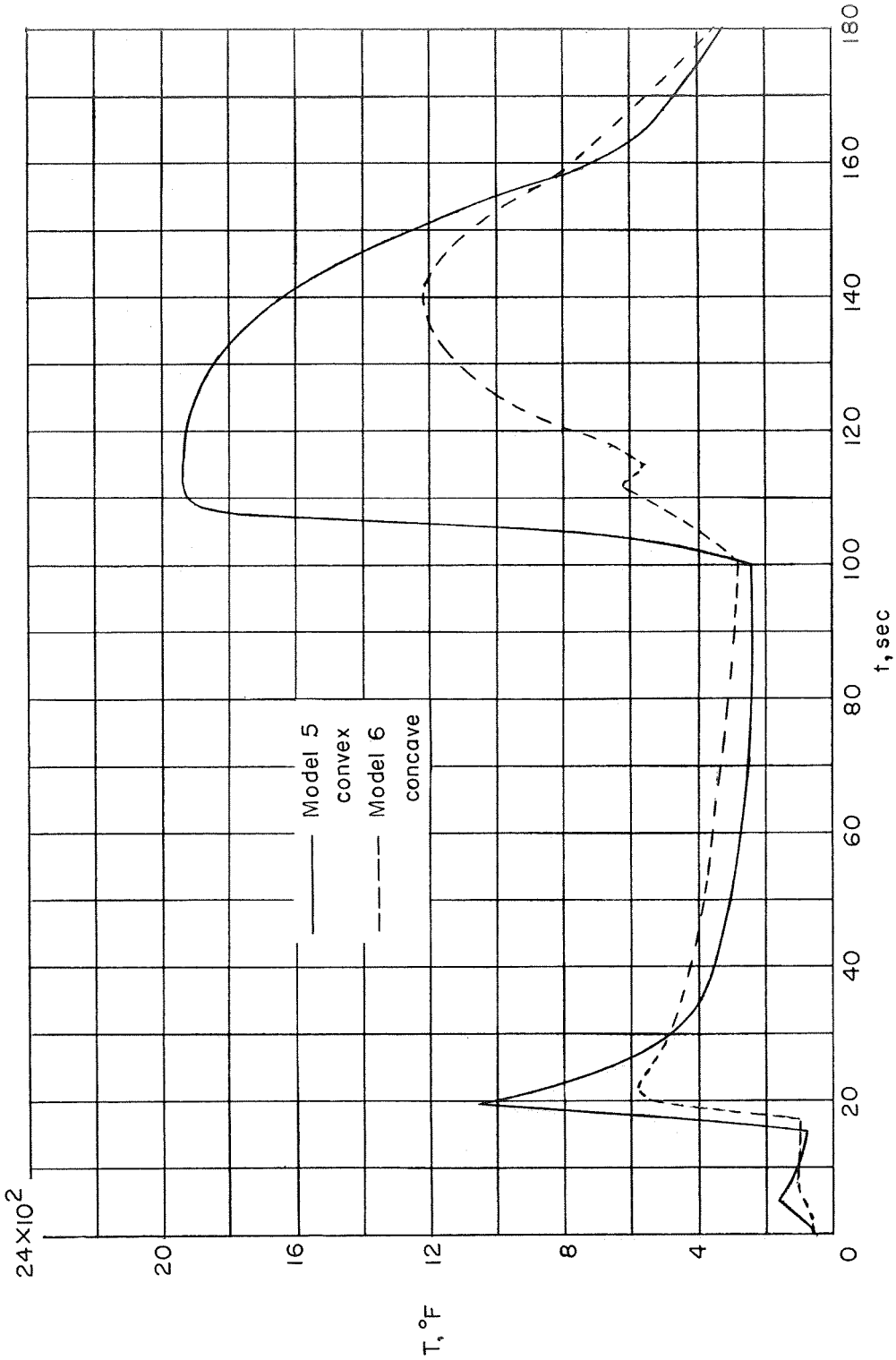

Figure 17.- Temperature histories at the stagnation points of models 5 and 6.

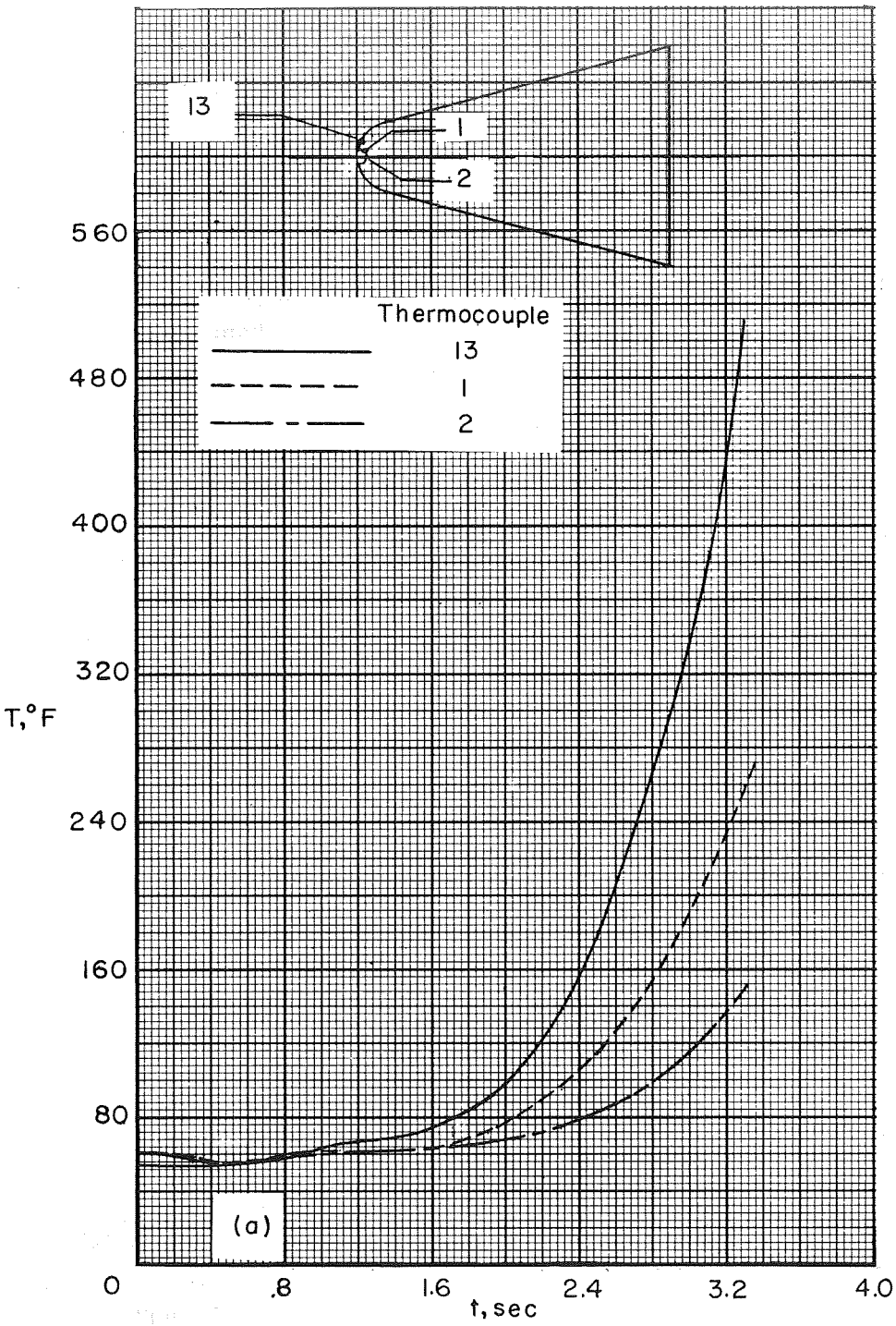

Figure 18.- Comparison of temperatures within spherical depressions with temperatures at comparable locations on smooth surface for model 7.

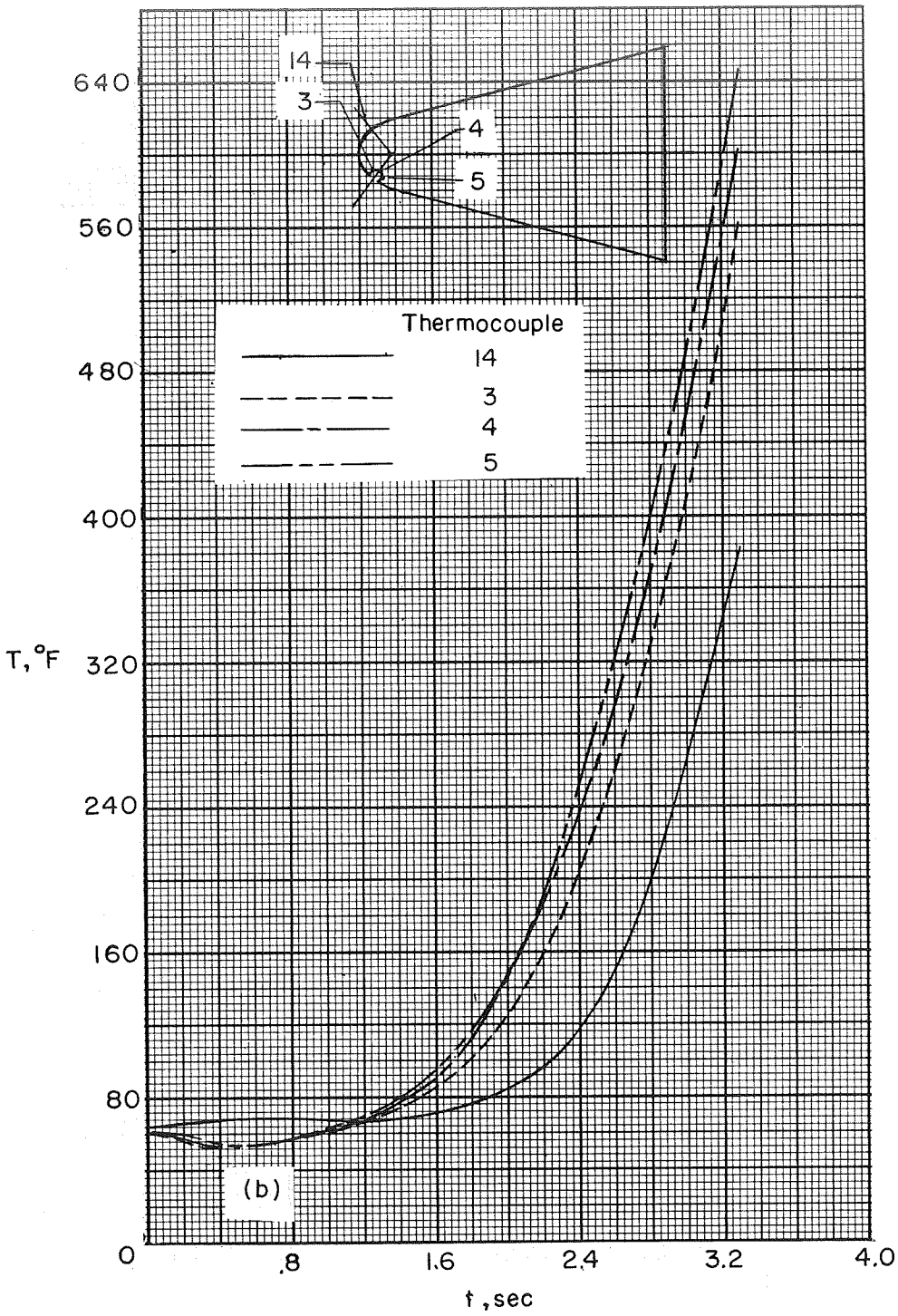

Figure 18.- Continued.

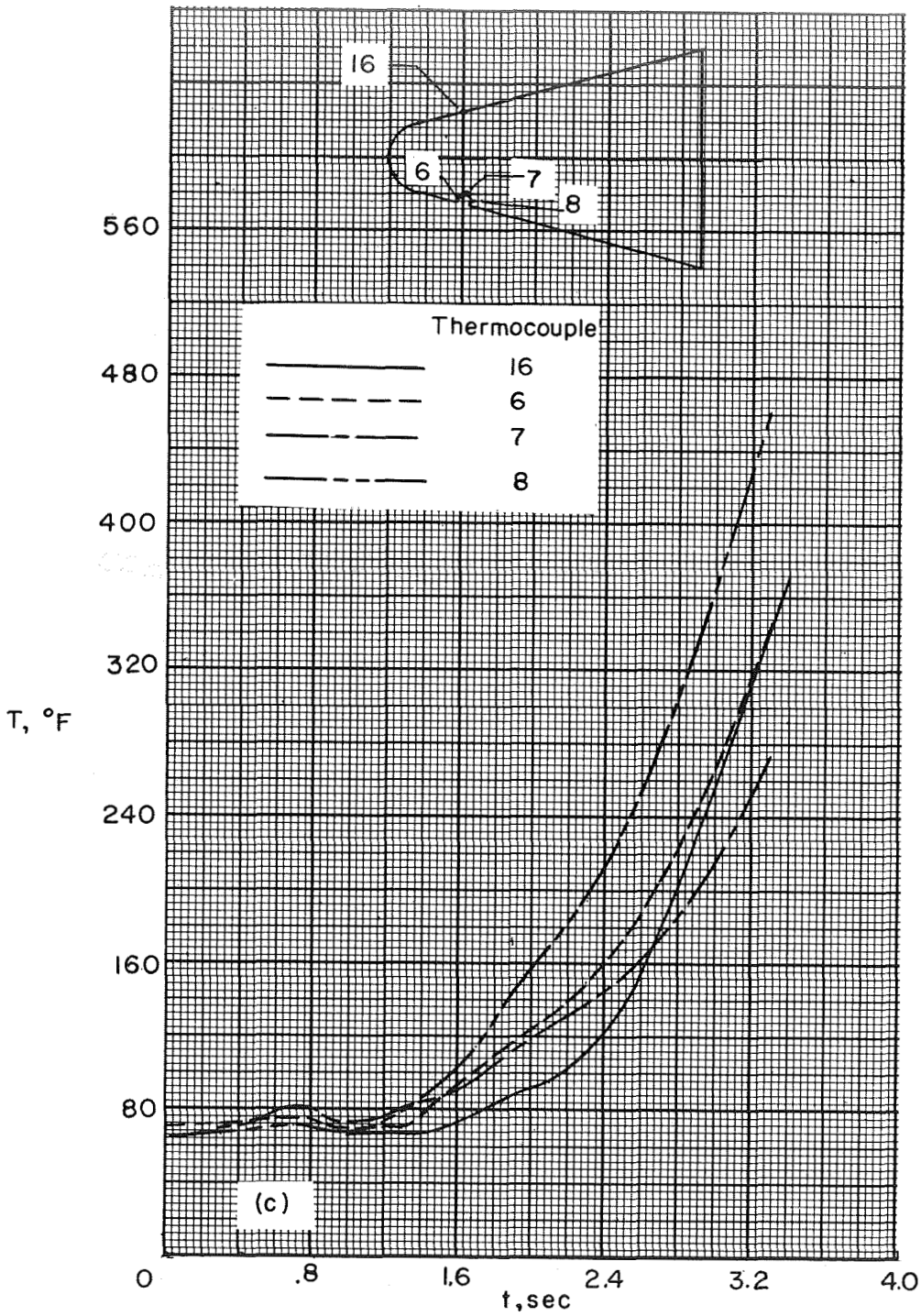

Figure 18.- Continued.

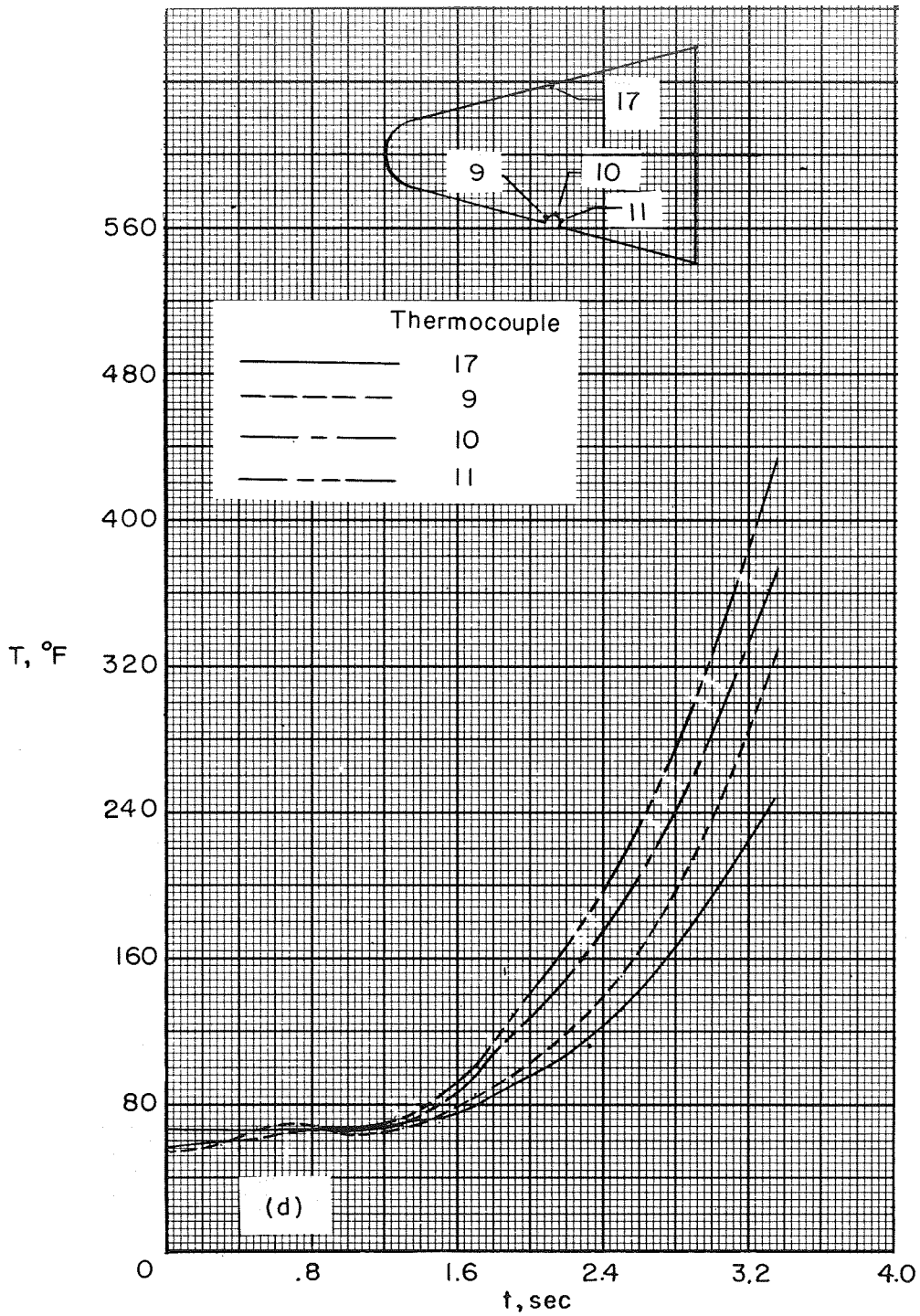

Figure 18.- Continued.

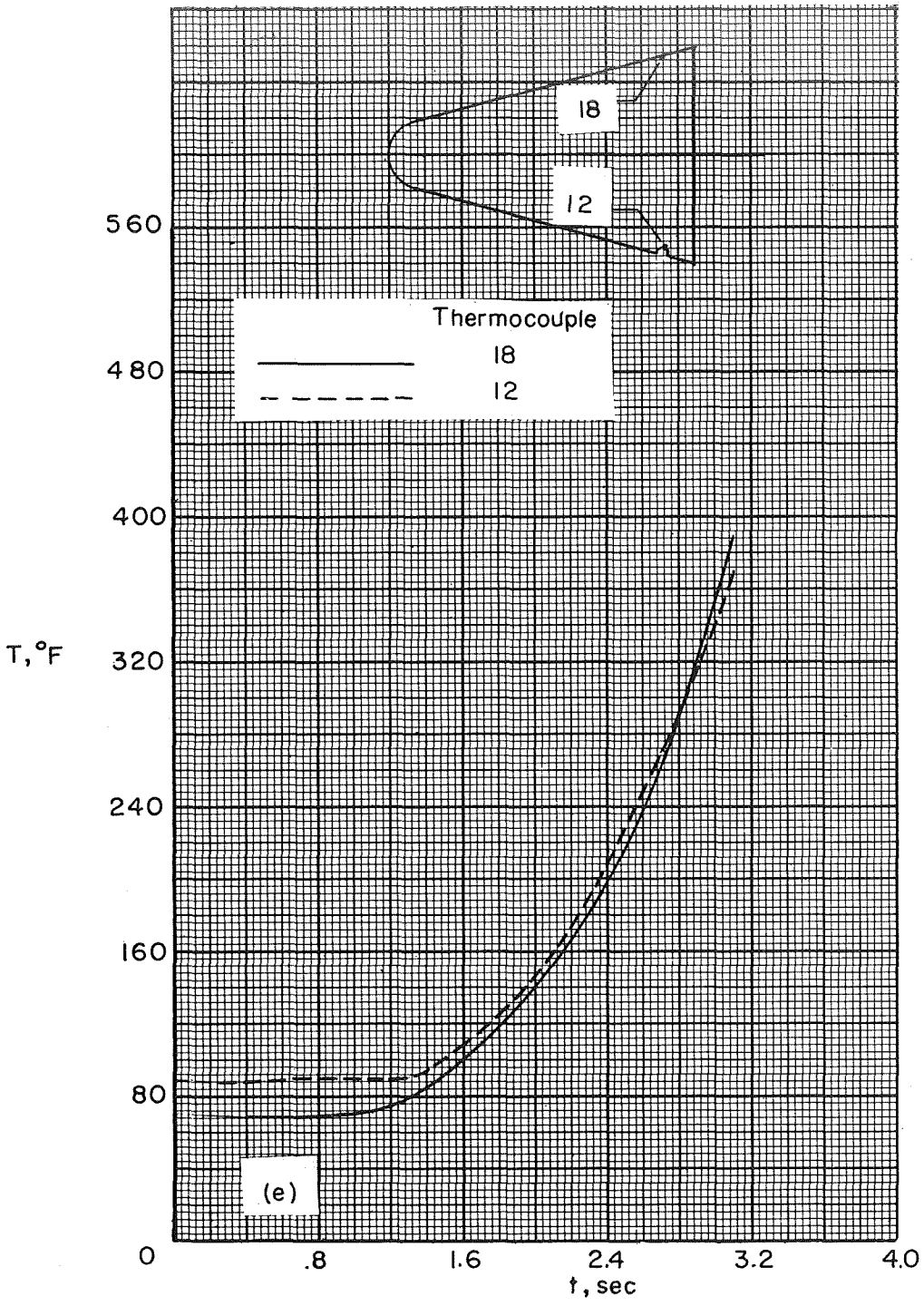

Figure 18.- Concluded.

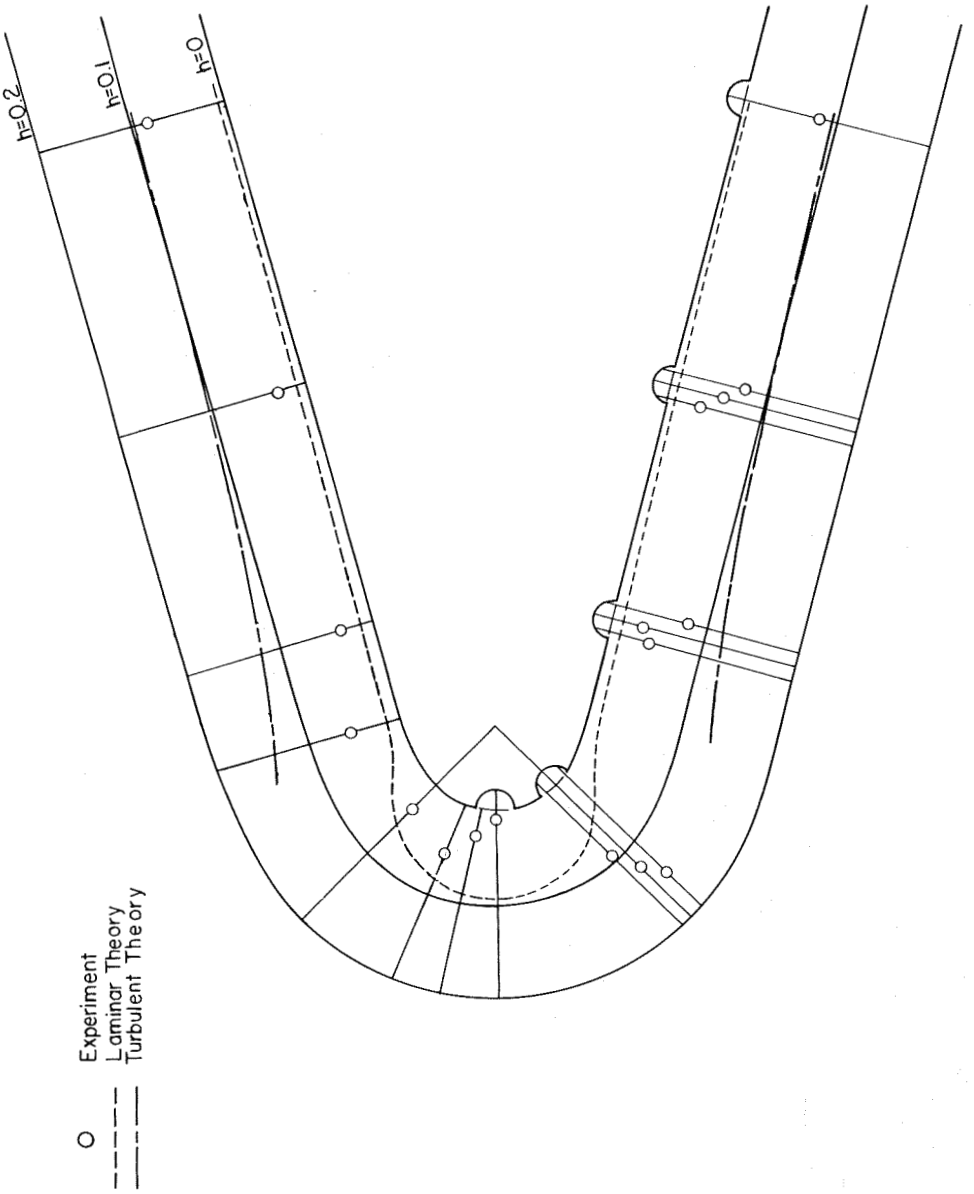

(a) t = 2.2 seconds; M = 1.99.

Figure 19.- Typical measured heat-transfer coefficients within spherical depressions compared with values at comparable locations on the smooth surface.

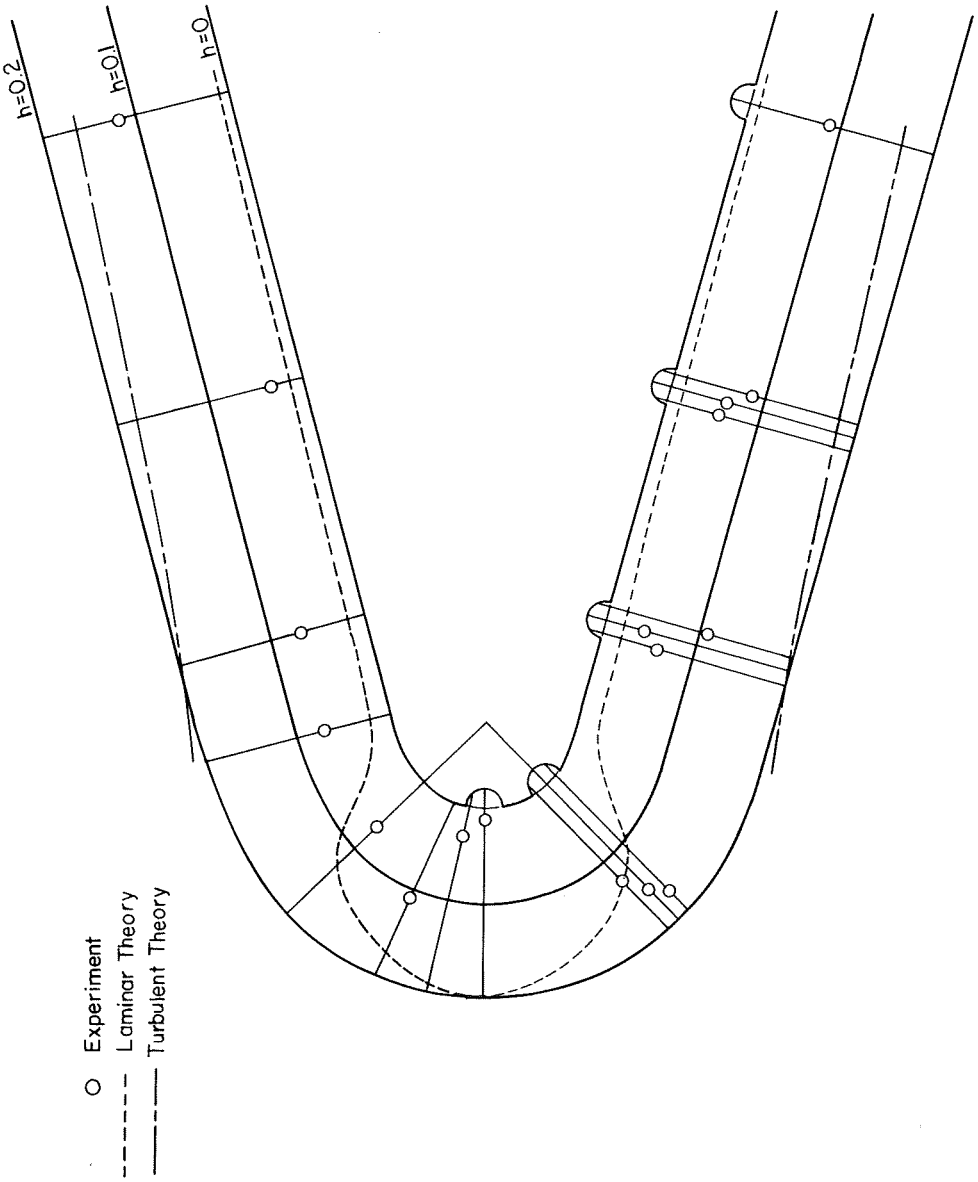

(b) t = 3.1 seconds; M = 3.05.

Figure 19.- Concluded.

CONFIDENTIAL

CONFIDENTIAL